Materials Today 91 (2025) 1–12

Contents lists available at ScienceDirect

Materials Today

journal homepage: www.elsevier.com/locate/mattod

A facile construction of LiF interlayer and F-doping *via* PECVD for LATP-based hybrid electrolytes: Enhanced Li-ion transport kinetics and superior lithium metal compatibility

Xian-Ao Li [a,1], Yiwei Xu [a,1], Kepin Zhu [a], Yang Wang [a], Ziqi Zhao [a], Shengwei Dong [b], Bin Wu [c], Hua Huo [b], Shuaifeng Lou [b], Xinhui Xia [d], Xin Liu [a,*], Minghua Chen [a,*], Stefano Passerini [e,f,g,*], Zhen Chen [a,*]

[a] Key Laboratory of Engineering Dielectric and Applications (Ministry of Education), School of Electrical and Electronic Engineering, Harbin University of Science and Technology, Harbin 150080, China
[b] Key Laboratory of Materials for New Energy Conversion and Storage (Ministry of Industry and Information Technology), School of Chemistry and Chemical Engineering, Harbin Institute of Technology, Harbin 150001, China
[c] School of Materials Science and Engineering, Nanyang Technological University, 50 Nanyang Avenue, Singapore 639798, Singapore
[d] College of Materials Science and Engineering, Zhejiang University of Technology, Hangzhou 310014, China
[e] Helmholtz Institute Ulm (HIU), Helmholtzstrasse 11, 89081 Ulm, Germany
[f] Karlsruhe Institute of Technology (KIT), 76021 Karlsruhe, Germany
[g] Austrian Institute of Technology (AIT), Center for Transportation Technologies, Giefinggasse 4, 1210 Wien, Austria

ARTICLE INFO

Keywords:
PECVD technology
Interface buffer layer
F-doping
Hybrid solid-liquid electrolyte
Superior electrochemical performance

ABSTRACT

Hybrid solid-liquid electrolytes show promise in resolving interfacial side reactions and poor electrode|electrolyte contact of solid-state batteries. However, the energy barrier between the liquid and the solid-state electrolytes impedes Li-ion migration, reducing Li^+ transport efficiency and overall battery performance. Here, we propose a modification strategy using plasma-enhanced chemical vapor deposition (PECVD) technology with fluoroethylene carbonate as the fluorine source, enabling *in situ* construction of a LiF buffer layer and F-doping on the $Li_{1.3}Al_{0.3}Ti_{1.7}P_3O_{12}$ (LATP) skeleton. Computational analyses reveal that F-doping activates additional Li-ion migration pathways, enhances ionic conductivity, and suppresses Li dendrite growth. The LiF layer prevents electron penetration and direct contact between LATP and Li metal, while also reducing the desolvation energy barrier to improve Li-ion transport across the solid|liquid interface with aids of F-doping. Consequently, Li||Li cells demonstrate stable cycling for 9000 h at 0.1 mA cm^{-2} and a critical current density of 2.2 mA cm^{-2}. Furthermore, full cells paired with $LiFePO_4$ and $LiNi_{0.8}Co_{0.1}Mn_{0.1}O_2$ cathodes retain 81.3 % and 67.2 % of their initial capacity after 300 cycles at 0.5 C. This study highlights the potential of PECVD technology for optimizing the interfaces of solid-state electrolytes, offering new insights into advancing next generation lithium metal battery performance.

Introduction

Since their commercialization in the 1990s, Li-ion batteries (LIBs) have profoundly reshaped the energy storage market [1,2]. In recent years, with the rapid expansion of the electric vehicle industry, the energy density of intercalation-based LIBs is gradually approaching its limit (300 Wh kg^{-1}), creating a bottleneck for extending vehicle driving range [3,4]. All-solid-state batteries (ASSBs) offer the advantages of high energy density and also enhanced safety, positioning them as promising candidates for the next generation of high-performance battery technology. Solid-state electrolytes (SSEs) are the core components of ASSBs, with inorganic oxide-based SSEs being particularly favored by their superior safety, chemical and thermal stability, mechanical strength, and high ionic conductivity. NASICON-type $Li_{1.3}Al_{0.3}Ti_{1.7}P_3O_{12}$ (LATP) electrolyte is undoubtedly one of the leading candidates [5–7]. However, the main challenge hindering the development of LATP is its

* Corresponding authors.
E-mail addresses: liu.xin@hrbust.edu.cn (X. Liu), mhchen@hrbust.edu.cn (M. Chen), stefano.passerini@kit.edu (S. Passerini), chen.zhen@hrbust.edu.cn (Z. Chen).
[1] These authors contributed equally: Xian-Ao Li and Yiwei Xu.

https://doi.org/10.1016/j.mattod.2025.10.003
Received 22 June 2025; Received in revised form 29 September 2025; Accepted 2 October 2025
Available online 13 October 2025

susceptibility to severe interface side reactions between Li metal and Ti^{4+}, which can damage the NASICON structure and ultimately lead to battery failure. Moreover, challenges at the solid-solid interface remain significant obstacles to their development and advancement at the current technological level [8–11]. To address the issue of poor interfacial wettability caused by the solid-solid contact, incorporating liquids into ceramic materials offers a viable solution [12]. Hybrid solid-liquid batteries — including semi- and quasi-solid-state types — combine the mechanical strength of solid electrolytes with improved interfacial contact from liquid components. This design suppresses lithium dendrites, enhances safety, and maintains compatibility with conventional LIB materials and processes, making it a practical transitional technology toward ASSBs. However, it still faces issues such as sluggish ion transport kinetics at the solid-liquid interface phase, which directly limits the performance ceiling of the battery system.

To address the issue of interface side reactions, researchers often construct an interface buffer layer to isolate Li metal, which can be broadly divided into inorganic- and polymer-based interface buffer layers [13–20]. Among these, LiF, featuring with superior interfacial stability, low electronic/ionic conductivity ratio and robust mechanical properties, is widely recognized as an excellent interlayer [21–24]. Although some SSEs exhibit ion conductivity comparable to that of liquid electrolytes (LEs), the energy barrier during Li^+ migration across the liquid|solid interface is substantial, leading to performance in hybrid solid-liquid systems that falls short of the anticipated levels. Thus, it is imperative to elevate the ion-conduction across the interfaces. Doping is also commonly used to enhance the ionic conductivity of LATP. Compared to the widely studied cation doping, anion doping has a smaller side effect on the structure, allowing for the regulation of intrinsic defect concentrations to improve ionic conductivity without affecting the lattice structure [25–27]. F-doping has been a primary focus in LATP anion doping [28,29], however, the underling mechanism is rarely reported.

Plasma technology leverages free radical chemistry, enabling chemical reactions that are otherwise impossible under standard conditions [30–32]. Plasma-enhanced chemical vapor deposition (PECVD) technology has been extensively adopted across diverse fields such as doping, deposition, and ionic vacancy generation. This technique is both energy-saving and highly efficient, with the entire process completed within a few minutes. Therefore, utilizing PECVD technology to stabilize the LATP|Li metal interface holds great potential. To the best of our knowledge, this technology has not yet been applied to the modification of SSEs.

Here, we developed, for the first time, an interfacial modification strategy that utilizes the fluoroethylene carbonate (FEC) solvent to treat the three-dimensional (3D) LATP skeleton *via* PECVD technology. This approach enables the simultaneous incorporation of fluorine into the LATP lattice and the *in situ* generation of a LiF protective layer on the skeleton surface. *Ab initio* molecular dynamics (AIMD) calculations on four different fluorine substitution structures reveal that F-doping activates potential Li-ion migration pathways at the sublattice scale within LATP, thereby enhancing its ionic conductivity. Additionally, the *in situ* generated LiF buffer layer effectively prevents electrons from passing through the bulk LATP. Notably, the reduced desolvation energy of Li^+ across LATP|LE interface significantly increases the proportion of Li^+ passing through the LATP phase. This synergy of enhanced Li^+ transport kinetics as well as protected Li|LATP interface contributes to substantially inhibited Li dendrites growth. As a result, Li||Li symmetric cells demonstrate an ultra-stable cyclability for over one year at 0.1 mA(h) cm^{-2}. When paired with $LiFePO_4$ (LFP) and $LiNi_{0.8}Co_{0.1}Mn_{0.1}O_2$ (NCM811) cathodes, the rate capability and cycling stability of full cells are greatly enhanced. This work validates its significance providing an efficient interface modification strategy and, more importantly, in highlighting the promising potential of PECVD technology for doping and interface modification of SSEs.

Results and discussion

Structural design and characterization of materials

The 3D LATP skeleton was fabricated *via* a template method, with the modification process shown in Fig. 1a. Under the strong applied electromagnetic field, FEC molecules undergo decomposition due to the bombardment by high-energy electrons, leading to the cleavage of C–F bonds and the generation of F free radicals. These highly active fluorine-containing intermediates, in conjunction with the energetic plasma environment, interact directly with the LATP surface. Upon collision with the LATP skeleton, the fluorine radicals incorporate into the lattice *via* chemical bonding, effectively inducing surface-level fluorine doping. Simultaneously, lithium-ions present on the LATP surface react with fluorine species to form a conformal LiF interfacial layer. This process enables the concurrent realization of fluorine doping within the LATP lattice and the formation of a robust, uniform LiF layer at the interface. The resulting sample is denoted as F-LATP. Scanning electron microscopy (SEM) image clearly shows the porous structure of LATP, while corresponding energy dispersive X-ray spectroscopy (EDS) mapping results demonstrate the uniform distribution of O, Al, Ti, F, and P elements (**Supplementary Fig. 1**). This is further supported by EDS elemental mapping obtained from scanning transmission electron microscopy (STEM) (Fig. 1b). The selected area electron diffraction (SAED) pattern (Fig. 1c) and the high-angle annular dark-field (HAADF) STEM image (Fig. 1d) both reveal the characteristic NASICON-type hexagonal structure (*R-3c*) of LATP [33,34]. X-ray diffraction (XRD) patterns of both LATP and F-LATP (**Supplementary Fig. 2**) also display the ideal NASICON phase of $LiTi_2(PO_4)_3$ (crystal card: PDF 35–0754). This could be primarily due to the low F-doping content in the LATP lattice.

To gain more insights into the chemical bonding environments, electron energy loss spectroscopy (EELS) and X-ray photoelectron spectroscopy (XPS) analyses were further carried out. As presented in Fig. 1e, the detection of Ti-L_1 and $M_{2,3}$ edges confirms the presence of Ti [35]. Additionally, the small pre-peak observed at 532 eV for F-LATP is attributed to the substitution of oxygen within the $(Ti/Al)O_6$ polyhedra [36]. This substitution modifies the electronic environment of oxygen, resulting in hybridization between the O-K conduction band and the unoccupied Ti 3d band, thereby generating additional occupied states. Electron paramagnetic resonance (EPR) spectroscopy was performed to characterize the oxygen vacancies in LATP before and after PECVD treatment. The *g* factor with a value of 2.004 is associated with oxygen vacancies [37,38]. The notable overlap in data suggests that high-energy ion bombardment does not result in the formation of additional oxygen vacancies in LATP (**Supplementary Fig. 3**). In the F 1s XP spectrum depicted in **Supplementary Fig. 4**, the distinct peak at approximately 685.1 eV corresponds to Li–F bonds, indicating the formation of surface LiF [39]. Additionally, the presence of Al–F, Ti–F, and P–F bonds observed in F 1s, Al 2p, Ti 2p and P 2p XP spectra (Fig. 1f and **Supplementary Fig. 4**) verifies the successful surface F-doping by PECVD.

Solid-state nuclear magnetic resonance (ssNMR) spectroscopy was employed to investigate the chemical environments of Al and P in the LATP and F-LATP samples. As shown in **Supplementary Fig. 5**, the ^{27}Al (spin I = 5/2) is mainly centered around −15 ppm, corresponding to the AlO_6 octahedral structure, which indicates that Al substitutes for Ti in TiO_6 [40]. Additionally, ^{31}P (spin I = 1/2) ssNMR spectrum exhibits a main peak of PO_4 (−27.8 ppm), along with peaks of $P(OTi)_4$ (−26.8 ppm), $P(OTi)_3(OAl)$ (−25.5 ppm), $P(OTi)_2(OAl)_2$ (−24.7 ppm) and $P(OTi)(OAl)_3$ (−23.6 ppm), which increases the total width and asymmetry of the signal [41,42]. Through comparing the ssNMR spectra before and after PECVD treatment, it is seen that F-doping affects the secondary structural units of LATP, leading to reduced overall peak intensity and broadened peak width. Due to the limited extent of F-doping, however, the peak positions in the ssNMR spectra remain nearly unchanged.

Subsequently, fresh lithium metal was brought into contact with the

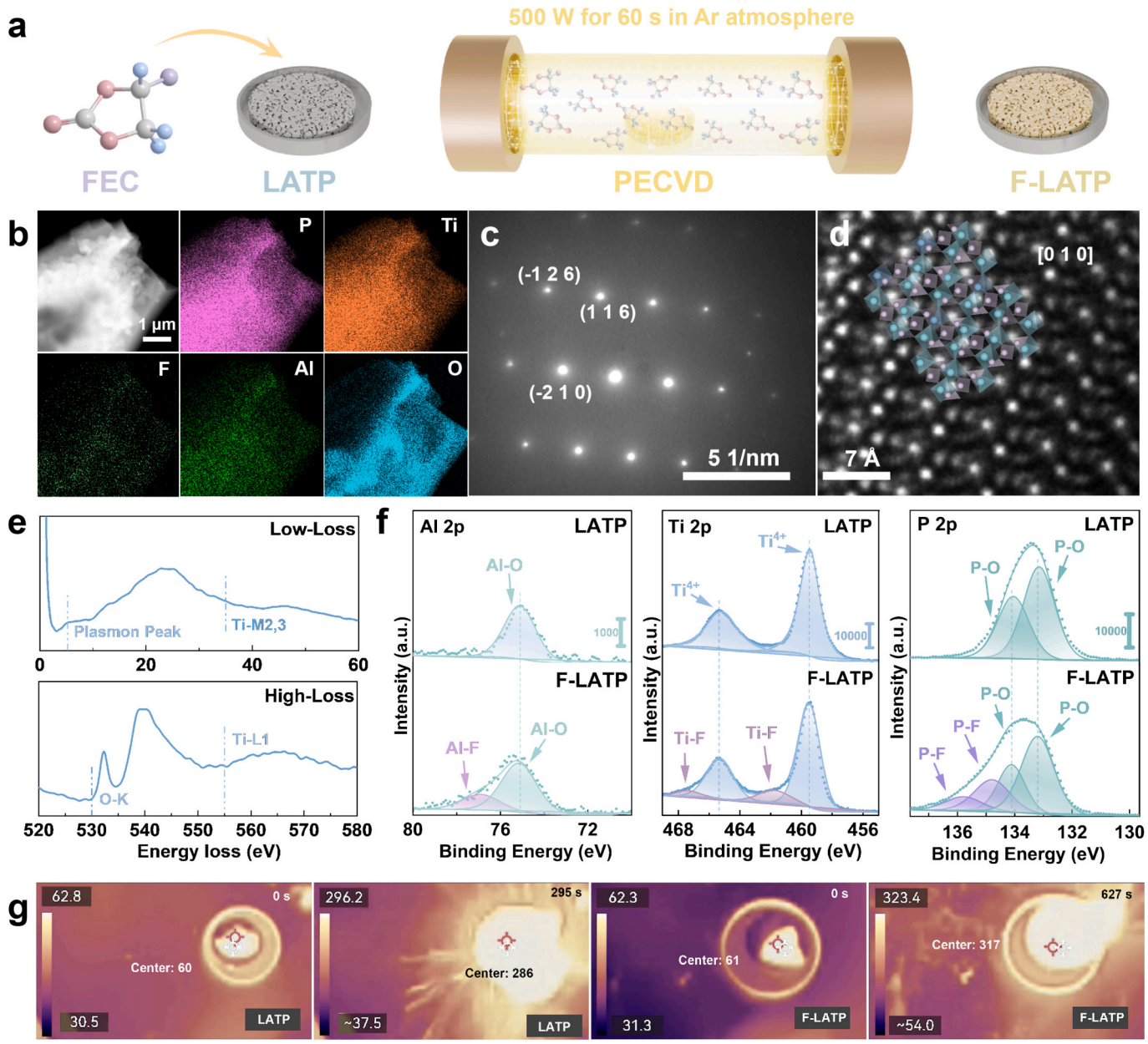

Fig. 1. Modification process and characterization of 3D F-LATP skeleton. a, Schematic illustration of F-LATP preparation route. b, STEM image of F-LATP skeleton with corresponding EDS mapping for P, Ti, F, Al and O elements. c, SAED pattern, d, HAADF image (deep blue: Al, cyan: Ti, and purple: P), and e, EELS spectra of F-LATP. f, XPS profiles of Al 2p, Ti 2p and P 2p for LATP and F-LATP skeletons. g, Thermal imaging captioning the thermal runaway behavior for LATP and F-LATP.

electrolyte skeleton and heated on a hot plate to 300 °C to evaluate the thermal and chemical stability of the modified F-LATP skeleton toward lithium metal after this strategic modification. Even under an Ar atmosphere, pristine LATP skeleton underwent thermal runaway after 295 s, leading to intense combustion. In sharp contrast, F-LATP skeleton exhibits significantly delayed thermal runaway, occurring after 627 s of heating (Fig. 1g, **Video S1**, **Video S2**). The LiF protective layer on the F-LATP surface effectively blocks its direct contact with Li metal. Moreover, F-doping is expected to help enhance the structural stability of the LATP skeleton [43,44]. Especially under heating conditions, the aforementioned dual modification effects significantly remit the thermodynamic instability issues caused by direct contact and redox response. To further validate the effectiveness of this modification strategy, the chemical stability of dense LATP pellets before and after fluorination (P_LATP and P_F-LATP) was evaluated under identical conditions. The results reveal that the thermal runaway time of fluorinated pellets was almost doubled (**Supplementary Fig. 6**, **Video S3**, **Video S4**), demonstrating that surface fluorination significantly enhances both the thermal stability and chemical stability of LATP.

Mechanistic investigation of F-doping via theoretical simulations

To fully elucidate the effect of F-doping in LATP, theoretical calculation and simulation analyses were conducted. The initial configuration of LATP was determined based on the XRD results (**Supplementary Fig. 7a**). The most stable $Li_{1.3}Al_{0.3}Ti_{1.7}P_3O_{12}$ configuration was selected as shown in **Supplementary Fig. 7b**. To investigate the effect of F substitution, one of the 72 oxygen atoms in the structure was replaced with F. Based on the crystal structure and atomic environment of LATP, four potential fluorine substitution sites were identified, F-1: LiO_6-AlO_6-PO_4, F-2: TiO_6-PO_4, F-3: LiO_6-TiO_6-PO_4, and F-4: AlO_6-PO_4, as illustrated in Fig. 2a. While all four F-doped configurations may coexist in

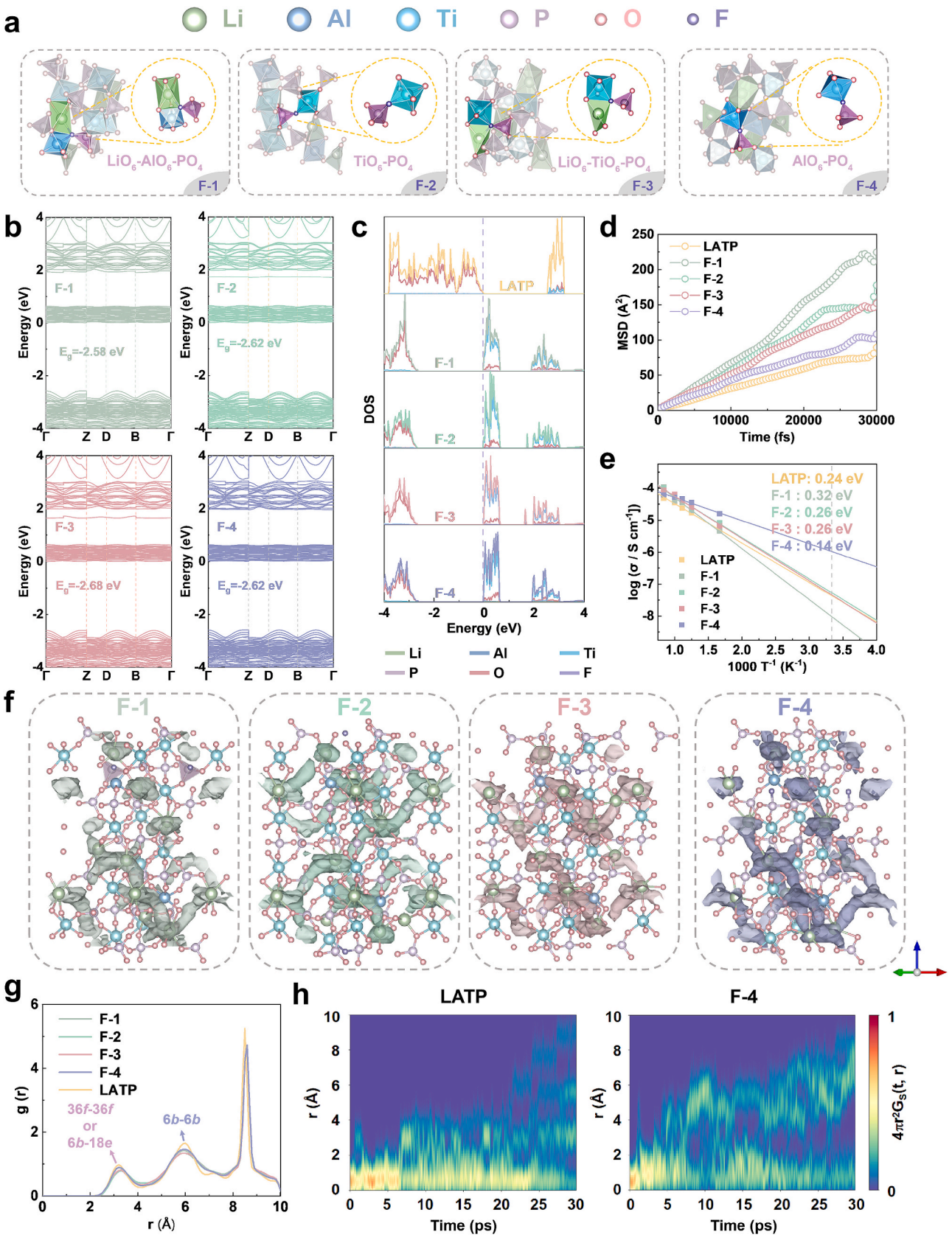

Fig. 2. The optimization mechanism analysis of F-doping. a, Visualization of the four distinct F-doping positions within the LATP structure. b, Band structure diagrams, c, DOS image (The colors at the bottom represent the partial density of states (PDOS) for each element.) d, MSD plot at 1200 K. e, Arrhenius plots. f, The probability density distribution map of Li-ions obtained from AIMD at 600 K. g, The RDFs plot of Li-Li interactions at 600 K. h, The distribution of the van Hove correlation function $G_s(r, t)$ for LATP and F-4.

actual LATP, precise control over specific doping sites within the crystal lattice remains challenging. First, the impact of F-doping on LATP was evaluated in terms of its band structure and density of states (DOS). The calculated band structures for F-LATPs are presented in Fig. 2b, while the band structure of pristine LATP is shown in **Supplementary Fig. 8**. The energy band gaps for LATP, F-1, F-2, F-3 and F-4 are −2.52, −2.58, −2.62, −2.68, and −2.62 eV, respectively. These results demonstrate that F-doping increases the band gap, thereby reducing the electronic conductivity of the material. This is further verified by DOS analysis (Fig. 2c). In addition, it is evident that the valence band in both pristine LATP and F-LATPs is primarily contributed by the O. The conduction band of LATP is jointly contributed by both O and Ti. However, in F-LATP, the conduction band is predominantly contributed by the Ti. This indicates that after F-doping, Ti plays a more significant role in the conduction process, which may alter the overall electronic properties and conduction behavior of the material.

To investigate F-doping effect on Li diffusion, AIMD calculations were performed. The mean square displacement (MSD) diagram at 1200 K is shown in Fig. 2d, while MSD diagrams for other temperatures are provided in **Supplementary Fig. 9**. Notably, the Li-ion diffusion coefficient increases after F-doping. Arrhenius plot (Fig. 2e) was analyzed to further evaluate the effect of F-doping on ionic conductivity and activation energy in LATP. Extrapolating from the Arrhenius relationship, the ionic conductivities at 300 K for the pristine LATP and F-doped LATPs (F-1, F-2, F-3, and F-4) were calculated to be 1.59 (LATP), 0.38 (F-1), 1.97 (F-2), 1.68 (F-3), and 38.33 (F-4) mS cm^{-1}, respectively. Most of the F-doped sites exhibit an enhancement in ionic conductivity, which aligns with experimental findings that F-doping improves the ionic conductivity of LATP. The activation energies for LATP, F-1, F-2, F-3, and F-4 were calculated to be 0.24, 0.32, 0.26, 0.26, and 0.14 eV, respectively. Notably, the F-4 structure exhibits a significantly lower activation energy. Even if all four F-doped configurations coexist within the actual LATP system, the pivotal role exerted by the F-4 structure can still endow the F-doped LATP with a higher ionic conductivity and a lower activation energy in comparison to LATP. To further explore the diffusion pathways and mechanisms of Li-ions, at 600 K, the probability density distributions of Li-ions in F-LATPs and LATP are demonstrated in Fig. 2f and **Supplementary Fig. 10**, respectively. The interstitial Li-ion diffusion mechanism is clearly evidenced. In contrast to the pristine LATP, where Li-ions primarily diffuse through unidirectional channels, F-doping activates interconnected channels, forming a 3D diffusion network (**Supplementary Fig. 11**). This enhancement in ion migration rate is attributed to the activation of migration channels at the sublattice scale following F-doping.

Fig. 2g illustrates the radial distribution function (RDF) for Li-ions at 600 K, demonstrating attenuated peaks corresponding to Li-Li pair interactions at Wyckoff positions 36*f*-36*f* (or 6*b*-18*e*) and 6*b*-6*b* after F-doping. This observation signifies heightened Li-ion mobility. Additionally, the van Hove correlation function $G_s(r, t)$ was analyzed for both pristine LATP and F-doped LATPs, as shown in Fig. 2h and **Supplementary Fig. 12**. The function $G_s(r, t)$ gives the probability that the distance between the positions of the same particle at time t and t_0 is R. For undoped LATP, a peak appears between 0 and 2 Å with weak time dependence, indicating that atoms are more inclined to vibrate near the equilibrium position. In contrast, for F-doped LATPs, the peak intensity is significantly lower and becomes more dispersed over time, suggesting faster Li-ion migration capability compared to the undoped LATP.

Electrochemical characteristics of Li-ion transport kinetics

To assess the impact of this modification strategy on battery performance, hybrid ceramic-LE electrolytes were prepared and referred to as LATP-LE and F-LATP-LE, respectively. The electrochemical stability window (ESW) of LATP-LE and F-LATP-LE was evaluated in stainless steel (SS)||Li cells using linear sweep voltammetry at a scan rate of 0.2 mV s^{-1}, over a voltage range of −1 V to 6 V (**Supplementary Fig. 13**). The ESW of the F-LATP-LE system is nearly identical to that of the LATP-LE system. However, when the voltage exceeds the decomposition potential (4.75 V), the construction of the LiF interfacial layer and the effect of surface F doping effectively suppress the electrochemical reactions at the interface. This results in a significant reduction in the current within the F-LATP-LE system, demonstrating the positive effect of this strategy at the interface.

Fig. 3a shows the Arrhenius plots of LATP-LE and F-LATP-LE. At 25 °C, the ionic conductivities of these systems are 4.48×10^{-4} S cm^{-1} and 2.47×10^{-3} S cm^{-1}, respectively. Electrochemical impedance spectroscopy (EIS) plots measured at various temperatures are shown in **Supplementary Fig. 14**. Given the inherently high ionic conductivity of LE in hybrid solid-liquid systems, it is essential to assess the specific contributions to ion transport. To this end, we conducted a comparative analysis by separately evaluating the ionic conductivity of the LATP skeleton in two specific configurations: with lithium salt-free liquid electrolyte solvents (denoted as LATP-$Solvent_{50\ \mu L}$) and with excess LE (denoted as LATP-$LE_{150\ \mu L}$). To clearly compare the differences between LATP-LE system with different addition amounts of LE, we denote the LATP-LE systems mentioned earlier as LATP-$LE_{50\ \mu L}$ in this section. Evident from **Supplementary Fig. 15**, the LATP-$Solvent_{50\ \mu L}$ system, which reflects a single-ion conduction pathway *via* the LATP skeleton, exhibits an ionic conductivity of 1.38×10^{-4} S cm^{-1}. In addition, LATP pellets before and after surface fluorination were wet with 5 μL of LE (denoted as P_LATP-$LE_{5\ \mu L}$ and P_F-LATP-$LE_{5\ \mu L}$) and examined. Notably, the P_LATP-$LE_{5\ \mu L}$ system demonstrates a conductivity representative of solid-phase ion transport (*ca.*, 4.81×10^{-4} S cm^{-1}), whereas the P_F-LATP-$LE_{5\ \mu L}$ system showed an enhanced lithium-ion conductivity of 8.91×10^{-4} S cm^{-1}. This result further confirms the synergistic enhancement effect of this modification strategy on Li^+ transport performance. To comprehend this phenomenon, first, we performed a true density analysis of the LATP skeleton. Notably, the rather high value of 2.80 g cm^{-3} close to the theoretical density of 2.94 g cm^{-3}, suggests that a compact structure of 3D LATP skeleton is conducive to efficient ion transport. In contrast, the LATP-$LE_{150\ \mu L}$ system, in which excess LE forms more continuous pathways, achieves a significantly higher ionic conductivity of 1.56×10^{-3} S cm^{-1} (*vs.* 4.48×10^{-4} S cm^{-1} of LATP-$LE_{50\ \mu L}$). These results indicate that the ion conduction capability of LE within LATP skeleton only manifests when sufficient LE is present to form continuous ion transport channels throughout the composite.

To further validate this interpretation, we additionally measured the ionic conductivity of pure LE and LE confined within an inert MgO skeleton (MgO-LE). Digital photographs of the MgO skeleton (**Supplementary Fig. 16a, 16b**) reveal a disk of approximately 1.3 mm thickness and 16 mm diameter. To ensure scientific rigor, we introduced 85 μL of LE into the MgO skeleton, calculated based on its volume (0.2376 cm^3) and porosity (46.7 %). Owing to its relatively low true density (2.66 g cm^{-3} *vs.* 3.58 g cm^{-3} theoretical), the MgO skeleton allows for more accessible pore space for LE, enabling the formation of continuous LE transport channels even when LE is introduced in proportional amounts. As a result, the Nyquist plots of MgO-LE and pure LE exhibit similar impedance profiles, whereas those of LATP-LE and LATP pellets remain closely aligned, highlighting LATP-LE limited LE-based conduction. Notably, even when varying the LE content, the impedance profiles of MgO-LE remain comparable to those of the pure LE system (**Supplementary Fig. 16c**). The measured ionic conductivities further support this interpretation: pure LE and MgO-$LE_{85\ \mu L}$ exhibit high values of 1.19×10^{-2} S cm^{-1} and 3.56×10^{-3} S cm^{-1}, respectively — both significantly higher than those of the LATP-$LE_{50\ \mu L}$ (4.48×10^{-4} S cm^{-1}) and LATP pellet systems (4.81×10^{-4} S cm^{-1}). A statistical comparison of ionic conductivity across systems (**Supplementary Fig. 17**) reinforces these observations. Overall, these results confirm that the solid electrolytes, liquid electrolytes, and solid electrolyte|liquid electrolyte interface themselves are all involved in ion transport. Among these, the dominance of the liquid phase increases with the increasing content of liquid electrolytes. In hybrid solid-liquid systems with discontinuous

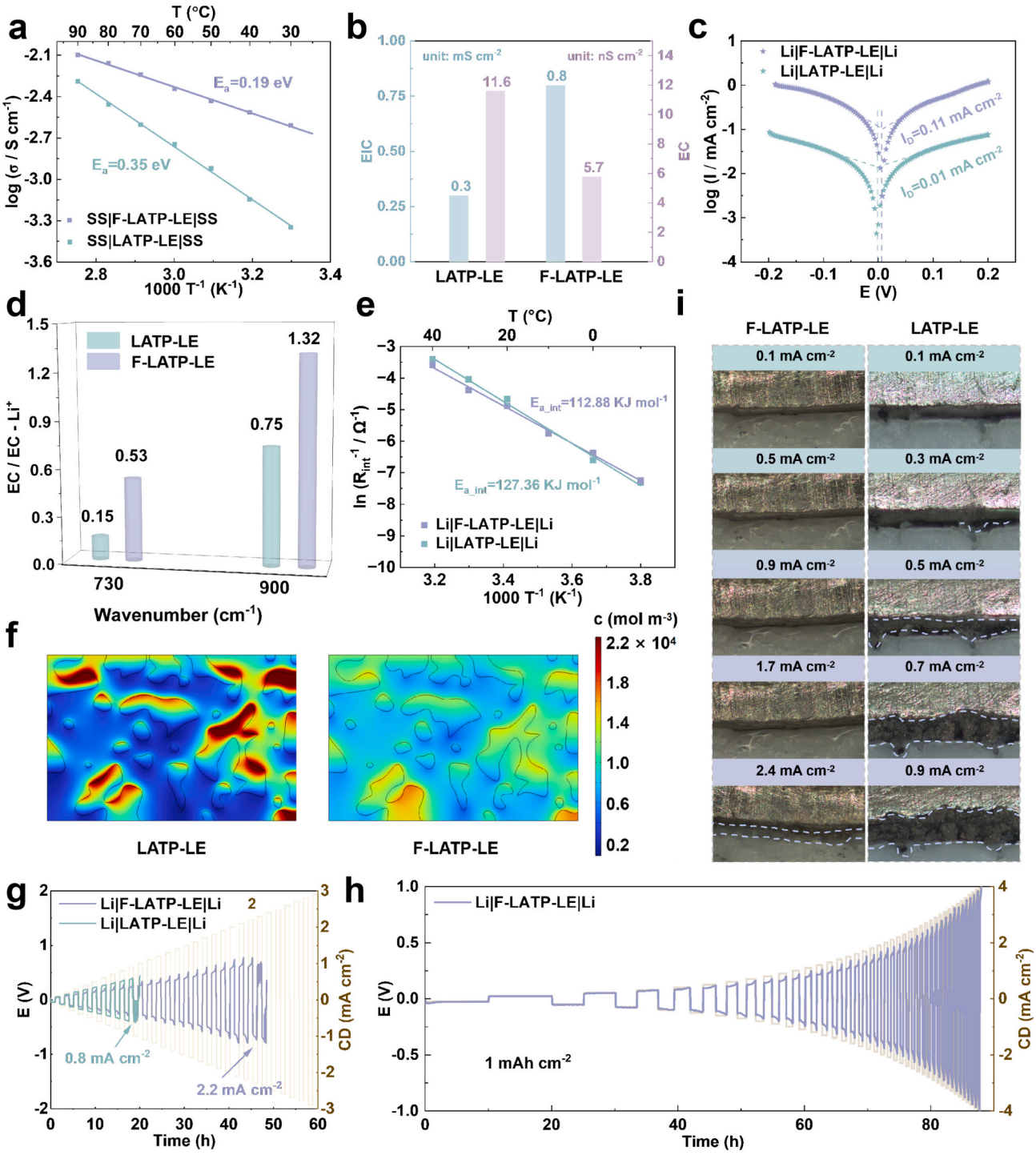

Fig. 3. Electrochemical analyses reveal the modification effects. a, Arrhenius plots of F-LATP-LE and LATP-LE. b, Comparison of EIC and EC between the two systems. c, Tafel curves of F-LATP-LE and LATP-LE. d, Ratio of free EC solvent to EC-Li^+ based on Raman spectroscopy data. e, Activation energy for Li-ions desolvation and interfacial migration. f, The concentration distribution map of Li^+ during the deposition process. CCD of the Li||Li cells in g, constant-time mode and h, constant-capacity mode (1 mAh cm^{-2}). i, OM snapshots illustrating lithium growth under varying current densities.

liquid-phase conduction, the solid electrolytes provide stable and indispensable ion conduction channel.

Furthermore, interfacial ion transport also plays a crucial role in determining overall performance. The activation energy across the solid-liquid interface for the F-LATP-LE system was calculated to be only 0.19 eV, which is significantly lower than that of the LATP-LE system (0.35 eV), consistently with our AIMD results. The Li^+ transference number (t_{Li}^+) is 0.32 for F-LATP-LE and 0.21 for LATP-LE (**Supplementary Fig. 18**), indicating that a larger proportion of Li^+ migrates through the solid electrolyte in the F-LATP-LE system along with faster kinetics. This improvement is attributed to higher ionic conductivity of F-LATP skeleton as well as reduced energy barrier at the liquid-solid interface, due to the LiF buffer layer and enhanced Li-ion transport kinetics after F-doping. Electronic conductivity (EC), critical for preventing the growth of Li dendrites [19], was measured (**Supplementary Fig. 19**). Thanks to the excellent electronic insulating

property of LiF, the F-LATP-LE exhibits a lower value compared to the LATP-LE counterpart, *ca.*, 5.78 × 10^{-9} *vs.* 1.16 × 10^{-8} S cm^{-1}. Fig. 3b compares the effective ionic conductivity (EIC) and EC of both systems. The synergistic effect between the interfacial and bulk phases results in a nearly tenfold enhancement in Li^+ ionic conductivity for F-LATP-LE, which is expected to facilitate rapid dis-/charge capability. Taken together, the substantially enhanced EIC and decreased EC demonstrate the effectiveness of this modification strategy.

To further examine Li-ion transport kinetics and interfacial charge transfer, Tafel plots of Li|F-LATP-LE|Li and Li|LATP-LE|Li cells were compared, as shown in Fig. 3c. The results reveal that the cell with the F-LATP-LE exhibits a significantly higher exchange current density (0.11 mA cm^{-2}) compared to the one employing LATP-LE (0.01 mA cm^{-2}). This substantial improvement demonstrates that the *in situ* generated LiF buffer layer effectively reduces interfacial impedance, thereby promoting faster charge transfer at the interface [45].

To investigate the influence of the LiF buffer layer and F-doping on the Li^+ bonding environment with LEs, Raman spectra of LATP and F-LATP pieces immersed in LEs were analyzed (**Supplementary Fig. 20**). Compared with LATP-LE, F-LATP-LE exhibits noticeable red shifts in the EC and EC-Li^+ peaks, attributed to altered interactions between the F-doped LATP skeleton and the solvent. This shift reflects weakened EC-Li^+ coordination, likely due to solvent ring deformation and electron redistribution at the interface [46]. Furthermore, integral area analysis reveals a notable increase in the ratio of free solvent to solvent-Li^+ complexes. This indicates a higher degree of free Li-ions, which is advantageous for homogenizing Li^+ flux (Fig. 3d) [47]. Typically, Li^+ needs to overcome a desolvation energy barrier (E_{a_int}) to cross the solid-liquid interface and enter into the ceramic skeleton. The E_{a_int} decreases from 127.36 KJ mol^{-1} to 112.88 KJ mol^{-1} after modification (Fig. 3e) [48]. To exclude the potential influence of complex interfacial effects inherent in the 3D skeleton, additional verification tests were conducted on P_LATP-$LE_{5\ \mu L}$ system and P_F-LATP-$LE_{5\ \mu L}$ system. According to **Supplementary Fig. 21**, a similar trend is evident, with a reduced E_{a_int} value from 77.95 KJ mol^{-1} to 64.63 KJ mol^{-1}. In case of the LATP-LE system, Li-ions preferentially migrate through the LE, while the LATP skeleton exhibits tortuous continuous pathways with numerous dead ends. This leads to ion accumulation in the enclosed regions of the skeleton, resulting in significant polarization. By contrast, F-LATP-LE not only exhibits reduced E_{a_int}, but also achieves significantly enhanced likelihood of Li^+ transport through the bulk LATP. Finite element simulations corroborate these findings by modeling Li^+ concentration and current density distribution in LATP-LE and F-LATP-LE systems (**Supplementary Fig. 22a**). As shown in Fig. 3f, the severe accumulated Li-ions within pores observed in LATP-LE is substantially mitigated after PECVD treatment, an indication of increased proportion of Li^+ passing through the ceramic skeleton and minimized polarization. Furthermore, uniform Li^+ flux achieved in F-LATP-LE reduces current density polarization within the system, which helps to prevent uneven Li deposition (**Supplementary Fig. 22b, 22c**).

Critical current density (CCD) serves as a benchmark for evaluating the suppression of Li dendrite growth, representing the maximum tolerable current density [49]. As shown in Fig. 3g, in constant-time mode, the LATP-LE cell experiences a short circuit at 0.8 mA cm^{-2}, whereas the F-LATP-LE cell maintains stability without short-circuiting up to 2.2 mA cm^{-2}. Additionally, in constant-capacity mode with a fixed capacity of 1 mAh cm^{-2}, the F-LATP-LE achieves a CCD of 4 mA cm^{-2} (Fig. 3h). In stark contrast, the LATP-LE only delivers a value of 0.6 mA cm^{-2} (**Supplementary Fig. 23**). Subsequently, the Li deposition behavior under varying current densities was studied using an *in situ* optical microscope (OM). As depicted in Fig. 3i, in the LATP-LE, fine Li wires form at a current density of 0.3 mA cm^{-2}, and a thick layer of dead Li appears at 0.7 mA cm^{-2}. In contrast, F-LATP-LE exhibits no visible dendritic Li growth until the current density reaches up to 2.4 mA cm^{-2}. This enhancement highlights the faster Li^+ transport kinetics and superior Li deposition behavior of the F-LATP-LE system, validating the effectiveness of this modification strategy in mitigating Li dendrite growth.

Evaluation of interfacial stability in symmetric cells

The cycling stability of Li|LATP-LE|Li and Li|F-LATP-LE|Li symmetric cells was evaluated by subjecting fresh cells to lithium stripping and plating test at 0.1 mA(h) cm^{-2}. As shown in Fig. 4a, the polarization voltage of Li|LATP-LE|Li gradually increases over time, but it suddenly drops after 2310 h due to cell short-circuiting. In contrast, the polarization voltage of Li|F-LATP-LE|Li remains below 1 V even after 9000 h of cycling. Impressively, the CCD and long-term cycling performance herein reported, to the best of our knowledge, represent the best results in the field of LATP interface modification (**Supplementary Fig. 24**).

To further investigate the mechanism behind these improvements, EIS measurement, a powerful non-invasive method that enables the capture of various relaxation processes, was performed [50]. Cyclic EIS tests were conducted upon lithium stripping-plating at 0.3 mA(h) cm^{-2} (**Supplementary Fig. 25**). The Li|LATP-LE|Li symmetric cell short-circuits after approximately 20 cycles due to severe interfacial side reactions, following an activation process of 10 cycles at 0.1 mA(h) cm^{-2}. The Nyquist plots measured before and after activation are shown in **Supplementary Fig. 26**. To analyze the impedance evolution upon cycling, Nyquist plots were recorded every 50 cycles up to 500 cycles (Fig. 4b). The Li|F-LATP-LE|Li symmetric cell exhibits minimal changes in impedance at the initial stages of cycling. However, over time, the impedance gradually increases, being the reason for the increased voltage polarization.

Subsequently, the EIS data were decoupled using distribution of relaxation times (DRT) analysis to gain insight into the microscopic physical and chemical behaviors at different relaxation times, thereby verifying the evolution mechanism of LiF buffer layer and F-doping [48]. Based on previous reports [51–53], the peaks at time constants ($\tau = RC$) of approximately 10^{-6} s, 10^{-5} s, and between 10^{-4} to 10^{-3} s correspond to the transport processes of Li-ions between the crystalline grain (R_{bulk}), grain boundary (R_{gb}), and Li|SSE-LE interface (R_{SEI}), respectively. Additionally, the peak observed between 10^{-5} to 10^{-4} s is attributed to the presence of the LiF buffer layer (R_{int}) [48]. As shown in Fig. 4c, while the LiF layer offers partial protection to the overall LATP, prolonged lithium stripping-plating at higher current densities lead to a gradual increase in R_{bulk} and R_{gb}, ultimately causing a deterioration in overall impedance. With the progression of cycles, the peaks of R_{SEI} and R_{int} tend to stabilize, suggesting that the *in situ* generated LiF gradually activates to form a stable interface. Fig. 4d provides a visual representation of the peak changes at these four positions. As the number of cycles increases, the stabilization of R_{SEI} and R_{int} peaks highlights the remarkable intrinsic stability of the interfacial layer achieved by this strategy.

For the investigation of the capability in inhibiting the reduction of Ti^{4+}, *ex situ* XPS analysis was performed to examine the chemical state of recovered LATP skeleton after 20 h of cycling in symmetric cells. As shown in Fig. 4e, the Ti 2p XP spectrum of recovered F-LATP exhibits only two peaks corresponding to Ti^{4+}, indicating that the LATP structure remains intact. Additionally, the Li 1s XP spectrum of cycled F-LATP reveals the presence of Li—F, confirming the stability of the buffer layer (**Supplementary Fig. 27**). In contrast, no Ti signals can be detected in case of the LATP recovered from cycled Li|LATP-LE|Li cell, predominantly due to the formation of thick reaction layer (**Supplementary Fig. 28**). This is further supported by the rough Li metal surface, along with visible cracks, and sharp, gravel-like Li dendrites (**Supplementary Fig. 29a**), which are clearly absent in case for the lithium metal recovered from cycled Li|F-LATP-LE|Li (**Supplementary Fig. 29b**).

To demonstrate the role of the LiF buffer layer in suppressing side reactions, the charge density difference at the LiF|LATP interface was calculated. This method visually reveals the flow of electrons following the interaction between the two interfaces [54]. As shown in Fig. 4f, there is a significant accumulation of positive charge at the LiF|LATP

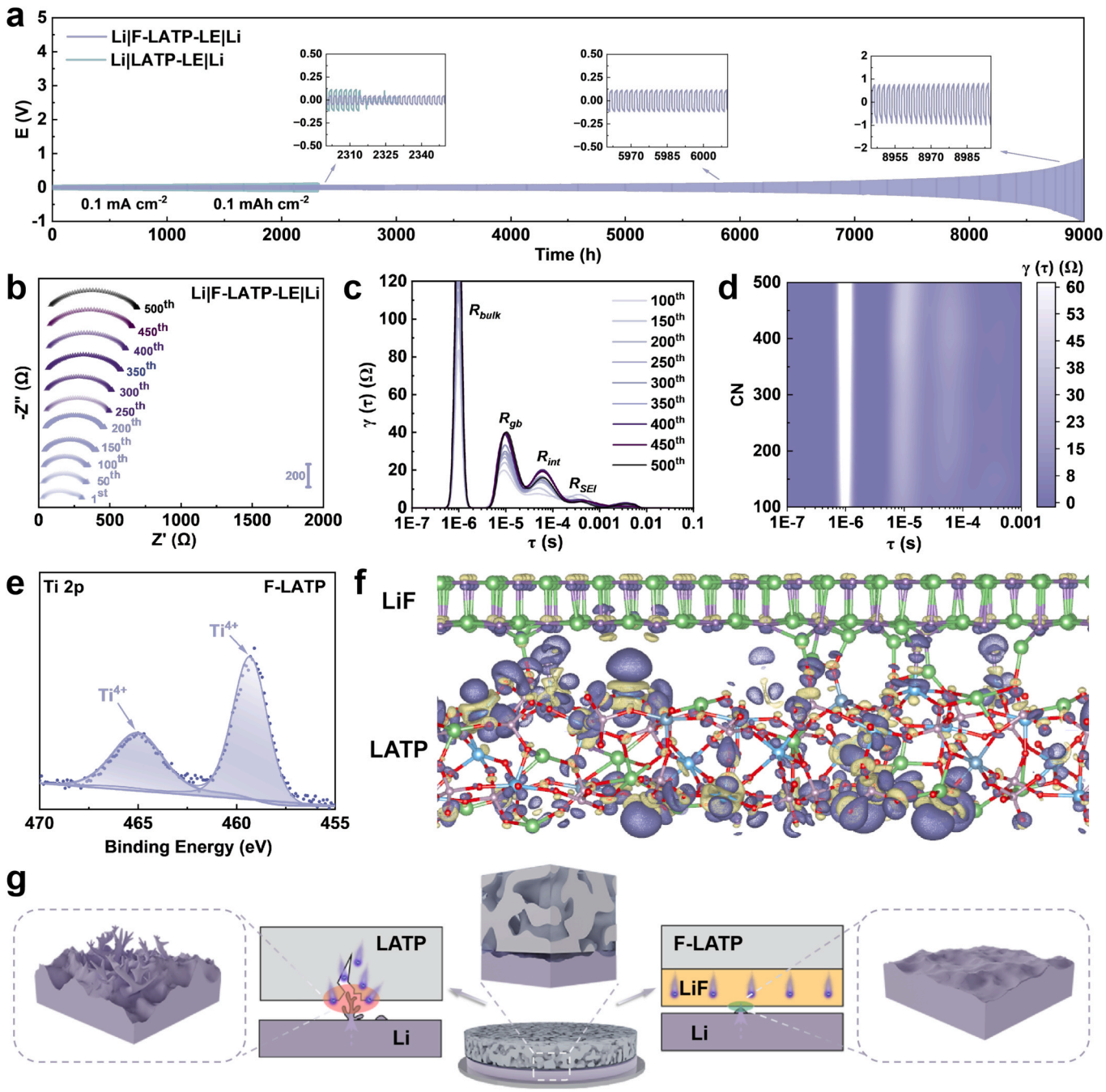

Fig. 4. Evaluation of interface stability in symmetrical cells. a, The cycling performance of Li symmetric cells cycled at 0.1 mA(h) cm^{-2} (with inset showing the magnified details). b, Nyquist impedance plots of F-LATP. c, DRT plot obtained by deconvolution of the EIS data shown in b. d, Contour map of the DRT data peak (CN: cyclic number). e, XP spectrum of Ti 2p in F-LATP after cycling. f, Charge density difference map (purple: positive electron cloud, yellow: negative electron cloud). g, Schematic diagram of the mechanism through which the LiF interface layer inhibits Li dendrite growth.

interface, indicating that electrons have difficulty in crossing the LiF buffer layer to reach the LATP. Due to its excellent electronic insulation properties, the LiF interfacial layer can significantly suppress the side reaction of LATP skeleton being reduced by metallic lithium. Moreover, LiF is known for its high Young's modulus of 69.9 GPa [55]. Thus, the electronic insulating property and robust mechanical performance of LiF buffer layer can effectively prevent interfacial side reactions and inhibit the growth of Li dendrites [56]. A schematic illustration of its role at the interface is shown in Fig. 4g, highlighting the significant impact of the LiF buffer layer in ensuring long-term cycling stability and preventing undesirable reactions that could compromise the overall electrochemical performance.

Electrochemical performance in full cell configurations

Building on these encouraging findings, we further examined the compatibility of the hybrid electrolytes with the mainstream cathode materials, LFP and NCM811, through cyclic voltammetry (CV) and galvanostatic cycling tests. The CV profiles obtained at 0.1 mV s^{-1} show a high degree of reversibility in both Li|LATP-LE|LFP and Li|F-LATP-LE|LFP cells (Fig. 5a). Notably, the latter exhibits higher peak currents with smaller redox peak potential differences, indicating faster Li^+ diffusion and lower polarization. However, CV tests at different sweep rates reveal significant distortion in the oxidation peaks of Li|LATP-LE|LFP as the sweep rate increases, reflecting intense side reactions and pronounced

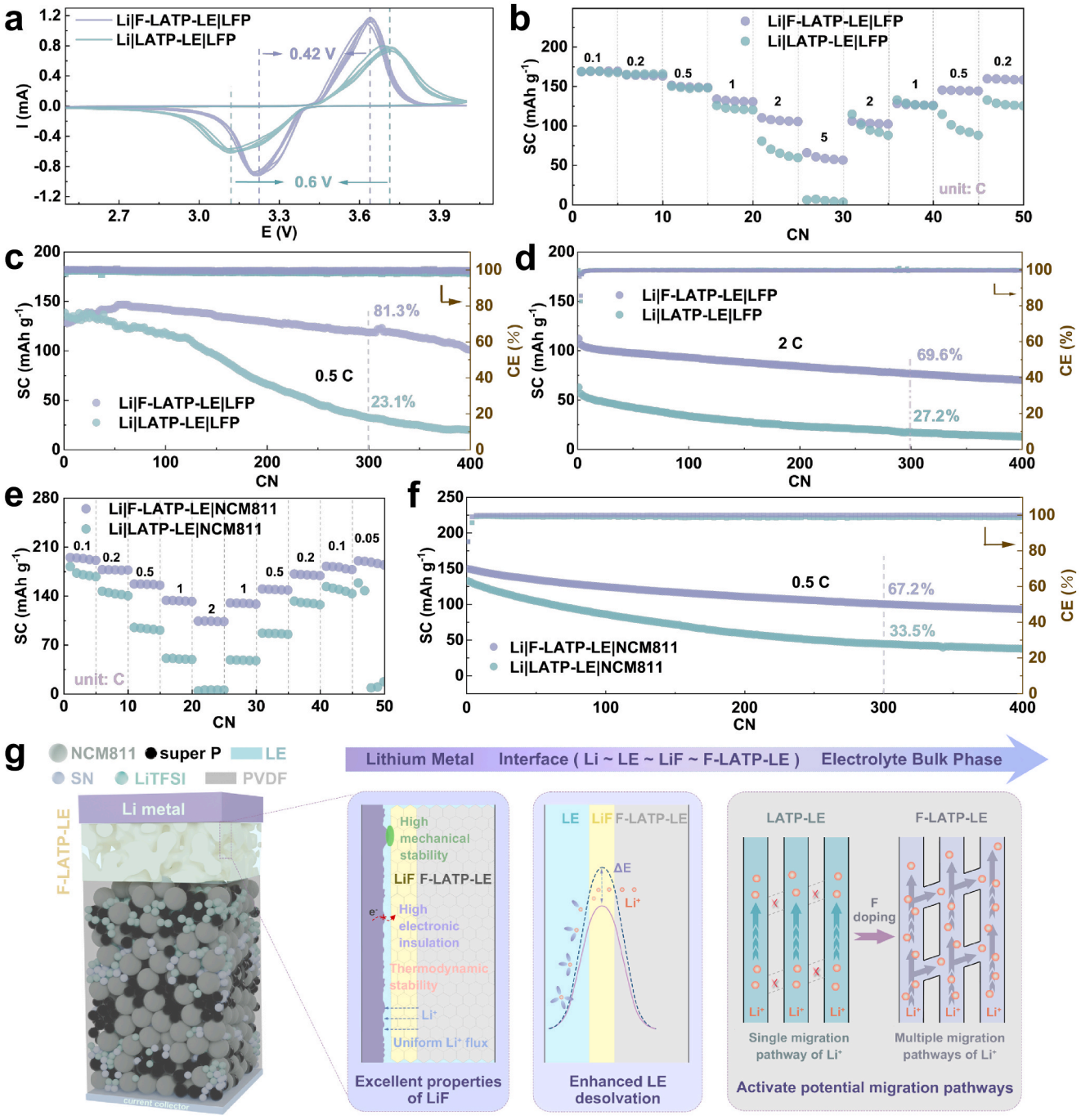

Fig. 5. Electrochemical performance of full cells paired with LFP and NCM811 cathodes. Comparative a, CV curves, b, Rate performance, and galvanostatic cycling performance at c, 0.5 C and d, 2 C of Li||LFP full cells. (SC: specific capacity, CE: coulombic efficiency). e, Rate performance and f, galvanostatic cycling performance at 0.5 C of Li||NCM811 full cells. g, Schematic diagram of the mechanism by which the LiF buffer layer and F-doping enhance the performance of the full cell.

irreversible capacity loss. In contrast, when pairing with F-LATP-LE as the electrolyte, full cells maintain well-defined peak shapes and higher peak currents, signifying that the modification effectively alleviates polarization while enhancing cell capacity and stability (**Supplementary Fig. 30**). Similarly, when F-LATP-LE and LATP-LE are paired with NCM811 cathodes, the Li|LATP-LE|NCM811 full cell shows poor reversibility in the first four cycles at a sweep rate of 0.1 mV s^{-1}. In contrast, the Li|F-LATP-LE|NCM811 full cell displays superior reversibility (**Supplementary Fig. 31a, 31b**). Furthermore, to further study the de-/lithiation kinetics of the systems, both cells were subjected to CV tests at different sweep rates (**Supplementary Fig. 31c, 31d**). The apparent diffusion coefficients of Li-ions using the Randles-Sevcik equation were calculated (**Supplementary Fig. 31e, 31f**) [57–59]. The results reveal a higher apparent Li^+ diffusion coefficient achieved in the Li|F-LATP-LE|NCM811 cell, with values for the de-/lithiation processes being 8×10^{-8} cm^2 s^{-1} and 5×10^{-8} cm^2 s^{-1}, respectively. This enhancement confirms that the LiF buffer layer and F-doping play a positive effect on Li^+ diffusion kinetics.

Rate capability tests demonstrate the superiority of the F-LATP-LE system (Fig. 5b). During the initial low-rate stage, both cells exhibit similar specific capacity (SC) values. However, above 0.5 C, the Li|F-LATP-LE|LFP cell demonstrates more distinct advantage upon increasing current densities. Specifically, only 5 mAh g^{-1} of capacity is delivered at 5 C, while the Li|F-LATP-LE|LFP cell delivers a capacity of

55 mAh g^{-1}. Furthermore, when the rate gradually returns to the initial value, the Li|F-LATP-LE|LFP cell shows much better reversibility, verifying its superior rate performance.

Fig. 5c compares the cycling performance of Li|F-LATP-LE|LFP and Li|LATP-LE|LFP full cells at 0.5 C. After 300 cycles, SC of the Li|LATP-LE|LFP cell decreases from an initial ~ 145 mAh g^{-1} to 33 mAh g^{-1}, corresponding a capacity retention rate of 23.1 %. In stark contrast, over the same period, 81.3 % of initial capacity is retained by the Li|F-LATP-LE|LFP full cell. Even after 400 cycles, this latter cell delivers a capacity of ~ 100 mAh g^{-1}, which is 5 times that of the Li|LATP-LE|LFP cell. Additionally, at 2 C, the Li|F-LATP-LE|LFP cell delivers an initial capacity of 112 mAh g^{-1}, and manages to remain 70.3 mAh g^{-1} capacity after 400 cycles, achieving a capacity retention ratio of 62.8 % (Fig. 5d). In comparison, the Li|LATP-LE|LFP cell delivers much lower initial capacity (62 mAh g^{-1}) and experiences stronger capacity decay, ending up with a capacity retention of only 20 %.

The rate performance of Li|F-LATP-LE|NCM811 and Li|LATP-LE|NCM811 full cells was also evaluated (Fig. 5e **and Supplementary Fig. 32**). At 0.1 C, the Li|F-LATP-LE|NCM811 cell exhibits a higher capacity, *ca.*, 194.9 *vs.* 181.8 mAh g^{-1} (Li|LATP-LE|NCM811). Even at a high rate (2 C), it still maintains a capacity of ~ 105 mAh g^{-1}. However, no capacity can be delivered at such a C-rate in case of the Li|LATP-LE|NCM811 cell, showcasing superior rate performance of Li|F-LATP-LE|NCM811. Additionally, a superiority in terms of cycling stability of Li|F-LATP-LE|NCM811 cell is revealed, evidenced by a much higher capacity retention ratio, *i.e.*, 67.2 % *vs.* 33.5 % (Li|LATP-LE|NCM811) after 300 cycles (Fig. 5f).

To investigate the compatibility of the F-LATP-LE system with high-mass-loading cathodes, LFP cathodes with increasing mass-loading were subjected to cycling at 0.5 C after initial activation cycles (**Supplementary Fig. 33**). After 100 cycles, the Li|F-LATP-LE|LFP cell with a ~ 10 mg cm^{-2} cathode retains 88.3 % of its initial capacity, significantly outperforming the Li|LATP-LE|LFP counterpart, which retains only 50.9 %. Remarkably, even at higher loadings of ~ 15 mg cm^{-2} and ~ 18 mg cm^{-2}, the F-LATP-LE-based cells maintain capacity retention ratios of 74.1 % (after 100 cycles) and 83.8 % (after 50 cycles), respectively. Furthermore, the Li|F-LATP-LE|LFP cells achieve superior rate capability even at a high mass-loading of ~ 15 mg cm^{-2}, recovering 93.6 % of its initial capacity at 0.5 C (*ca.*, 130.3 mAh g^{-1}) after undergoing high-rate cycling tests (up to 3 C) (**Supplementary Fig. 34**). These results showcase exceptional structural robustness and ion transport efficiency of F-LATP-LE, confirming its excellent compatibility and stability with high-loaded cathodes.

Based on these results, it can be concluded that modifying the LATP skeleton through PECVD technology significantly improves both the compatibility with Li and electrochemical performance within the cell system. The *in situ* generated LiF interfacial buffer layer plays a critical role by effectively preventing interfacial side reactions and suppressing the growth of Li dendrites. Additionally, the presence of LiF at the interface reduces the desolvation energy, facilitating smoother Li^+ transport. Moreover, the surface doping of fluorine into the LATP skeleton activates and expands potential migration pathways within the LATP bulk phase, enhancing the proportion of Li^+ transport through the bulk. These synergistic effects result in outstanding Li^+ transport kinetics, as depicted in the mechanism diagram in Fig. 5g. Collectively, these advancements enable the F-LATP-LE system to deliver exceptional electrochemical performance.

Conclusions

This study, for the first time, successfully developed a strategy for the simultaneous construction of interface LiF buffer layer and F-doping of LATP skeleton using PECVD technology. AIMD calculations reveal that F-doping activates potential Li-ion migration paths in the sub-lattice scale, contributing to enhanced ionic conductivity and deepening the understanding of how F-doping improves LATP's performance. The *in situ* generated LiF layer, which is electronically insulating, effectively mitigates side reactions at the Li|LATP interface. Furthermore, it significantly reduces desolvation energy, allowing for increased proportion of Li^+ migration through the solid phase. The combination of F-doping and LiF buffer layer markedly enhances interface stability and Li-ion transport kinetics. Consequently, the F-LATP-LE achieves 2.7 times higher effective ionic conductivity, and exhibits CCD values as high as 2.2 mA cm^{-2} (constant-time mode) and 4 mA cm^{-2} (constant-capacity mode). Notably, the Li|F-LATP-LE|Li symmetric cell operates impressively for 9000 h at 0.1 mA(h) cm^{-2} without short-circuiting. Furthermore, the hybrid electrolytes based on F-LATP-LE achieve superior rate capability and cycling stability when coupled with both LFP and NCM811 cathodes. While the full cell performance still has room for optimization, the strategy of simultaneously improving both the interface and bulk phase holds significant commercial potential. This work offers valuable insights into addressing challenges associated with SSEs and their interfaces with Li metal, paving the way for advancements in the development of next generation high-performance lithium metal batteries.

CRediT authorship contribution statement

Xian-Ao Li: Writing – review & editing, Writing – original draft, Visualization, Investigation, Data curation, Conceptualization. **Yiwei Xu:** Writing – review & editing, Writing – original draft, Visualization, Investigation, Data curation, Conceptualization. **Kepin Zhu:** Visualization, Investigation, Data curation. **Yang Wang:** Investigation, Data curation, Conceptualization. **Ziqi Zhao:** Visualization, Investigation, Data curation. **Shengwei Dong:** Writing – review & editing, Data curation. **Bin Wu:** Writing – review & editing, Formal analysis. **Hua Huo:** Writing – review & editing, Formal analysis. **Shuaifeng Lou:** Writing – review & editing, Formal analysis. **Xinhui Xia:** Writing – review & editing, Funding acquisition, Conceptualization. **Xin Liu:** Writing – review & editing, Methodology, Funding acquisition, Formal analysis, Conceptualization. **Minghua Chen:** Writing – review & editing, Project administration, Funding acquisition. **Stefano Passerini:** Writing – review & editing, Project administration, Formal analysis. **Zhen Chen:** Writing – review & editing, Project administration, Methodology, Funding acquisition, Formal analysis, Conceptualization.

Declaration of competing interest

The authors declare that they have no known competing financial interests or personal relationships that could have appeared to influence the work reported in this paper.

Acknowledgements

This work is supported by the National Natural Science Foundation of China (Grant No. 52277215, Grant No. 52377206 and Grant No. 52307237), the Postdoctoral Science Foundation of China (No. 2023M730884), and the Postdoctoral Science Foundation of Heilongjiang Province of China (LBH. Z23024), and the Natural Science Foundation of Zhejiang Province (Grant No. LD25E020003). The authors would like to acknowledge the Center for Electron Microscopy at Wuhan University for their substantial supports to TEM work. S. P. acknowledges the basic funding from the Helmholtz Association and the Austrian Institute of Technology. We appreciate SuanChou (suanchou.com) for the phase-field model.

Appendix A. Supplementary data

Supplementary data to this article can be found online at https://doi.org/10.1016/j.mattod.2025.10.003.

Data availability

Data will be made available on request.

References

[1] J. Choi, D. Aurbach, Promise and reality of post-lithium-ion batteries with high energy densities, Nat. Rev. Mater. 1 (2016) 16013, https://doi.org/10.1038/natrevmats.2016.13.

[2] X. Fan, et al., Non-flammable electrolyte enables Li-metal batteries with aggressive cathode chemistries, Nat. Nanotechnol. 13 (2018) 715–722, https://doi.org/10.1038/s41565-018-0183-2.

[3] A. Manthiram, X. Yu, S. Wang, Lithium battery chemistries enabled by solid-state electrolytes, Nat. Rev. Mater. 2 (2017) 16103, https://doi.org/10.1038/natrevmats.2016.103.

[4] Y. Hu, et al., Janus Electrolyte with modified Li^+ solvation for high-performance solid-state lithium batteries, Adv. Funct. Mater. 32 (2022) 2203336, https://doi.org/10.1002/adfm.202203336.

[5] K. Yang, et al., Progress and perspective of $Li_{1+x}Al_xTi_{2x}(PO_4)_3$ ceramic electrolyte in lithium batteries, InfoMat 3 (2021) 1195–1217, https://doi.org/10.1002/inf2.12222.

[6] P. Wu, et al., Recent advances in conduction mechanisms, synthesis methods, and improvement strategies for $Li_{1+x}Al_xTi_{2x}(PO_4)_3$ solid electrolyte for all-solid-state lithium batteries, Adv. Energy Mater. 13 (2023) 2203440, https://doi.org/10.1002/aenm.202203440.

[7] R. DeWees, H. Wang, Synthesis and properties of NaSICON-type LATP and LAGP solid electrolytes, ChemSusChem 12 (2019) 3713–3725, https://doi.org/10.1002/cssc.201900725.

[8] Y. Xiao, et al., Understanding interface stability in solid-state batteries, Nat. Rev. Mater. 5 (2020) 105–126, https://doi.org/10.1038/s41578-019-0157-5.

[9] J. Janek, W. Zeier, Challenges in speeding up solid-state battery development, Nat. Energy 8 (2023) 230–240, https://doi.org/10.1038/s41560-023-01208-9.

[10] Z. Tong, et al., Interface between solid-state electrolytes and Li-metal anodes: issues, materials, and processing routes, ACS Appl. Mater. Interfaces 12 (2020) 47181–47196, https://doi.org/10.1021/acsami.0c13591.

[11] S. Lou, et al., Interface issues and challenges in all-solid-state batteries: lithium, sodium, and beyond, Adv. Mater. 33 (2021) 2000721, https://doi.org/10.1002/adma.202000721.

[12] S. Pervez, et al., Overcoming the interfacial limitations imposed by the solid-solid interface in solid-state batteries using ionic liquid-based interlayers, Small 16 (2020) 2000279, https://doi.org/10.1002/smll.202000279.

[13] Y. Kim, et al., Anode-less seawater batteries with a Na-ion conducting solid-polymer electrolyte for power to metal and metal to power energy storage, Energy Environ. Sci. 15 (2022) 2610–2618, https://doi.org/10.1039/D2EE00609J.

[14] W. Kong, et al., Stabilizing $Li_{1.3}Al_{0.3}Ti_{1.7}(PO_4)_3$|Li metal anode interface in solid-state batteries by kevlar aramid nanofiber-based protective coating, Adv. Funct. Mater. 33 (2023) 2306748, Doi: 10.1002/adfm.202306748.

[15] D. Ding, et al., Stabilizing a $Li_{1.3}Al_{0.3}Ti_{1.7}(PO_4)_3$/Li metal anode interface in solid-state batteries with a LiF/Cu-rich multifunctional interlayer, Chem. Sci. 15 (2024) 3730–3740, https://doi.org/10.1039/D3SC06347J.

[16] L. Luo, et al., Solid-state lithium batteries with ultrastable cyclability: an internal-external modification strategy, ACS Nano 18 (2024) 2917–2927, https://doi.org/10.1021/acsnano.3c07306.

[17] L. Luo, et al., Insights into the enhanced interfacial stability enabled by electronic conductor layers in solid-state Li batteries, Adv. Energy Mater. 13 (2023) 2203517, https://doi.org/10.1002/aenm.202203517.

[18] Y. Liu, et al., Germanium thin film protected lithium aluminum germanium phosphate for solid-state Li batteries, Adv. Energy Mater. 8 (2018) 1702374, https://doi.org/10.1002/aenm.201702374.

[19] X. Hao, et al., Constructing multifunctional interphase between $Li_{1.4}Al_{0.4}Ti_{1.6}(PO_4)_3$ and Li metal by magnetron sputtering for highly stable solid-state lithium metal batteries, Adv. Energy Mater. 9 (2019) 1901604, Doi: 10.1002/aenm.201901604.

[20] Q. Cheng, et al., Stabilizing solid electrolyte-anode interface in Li-metal batteries by boron nitride-based nanocomposite coating, Joule 3 (2019) 1510–1522, https://doi.org/10.1016/j.joule.2019.03.022.

[21] X. Wang, et al., Electro-chemo-mechanical design of buffer layer enhances electrochemical performance of all-solid-state lithium batteries, Adv. Energy Mater. 15 (2024) 2402731, https://doi.org/10.1002/aenm.202402731.

[22] X. Shi, et al., In situ forming LiF nanodecorated electrolyte/electrode interfaces for stable all-solid-state batteries, Mater. Today Nano 10 (2020) 100079, https://doi.org/10.1016/j.mtnano.2020.100079.

[23] X. Fan, et al., Fluorinated solid electrolyte interphase enables highly reversible solid-state Li metal battery, Sci. Adv. 4 (2018) eaau9245, https://doi.org/10.1126/sciadv.aau9245.

[24] Y. Guo, et al., Fluorinating all interfaces enables super-stable solid-state lithium batteries by in situ conversion of detrimental surface Li_2CO_3, Adv. Mater. 36 (2024) 2308493, https://doi.org/10.1002/adma.202308493.

[25] T. Katsumata, et al., Development of electrochemical anion doping technique for expansion of functional material exploration, Adv. Funct. Mater. 33 (2023) 2307116, https://doi.org/10.1002/adfm.202307116.

[26] Q. Zhao, et al., Designing solid-state electrolytes for safe, energy-dense batteries, Nat. Rev. Mater. 5 (2020) 229–252, https://doi.org/10.1038/s41578-019-0165-5.

[27] C. Wang, et al., Ion hopping: design principles for strategies to improve ionic conductivity for inorganic solid electrolytes, Small 18 (2022) 2107064, https://doi.org/10.1002/smll.202107064.

[28] F. Yin, et al., Insight into the mechanism of Li ion diffusion in fluorine-doped $Li_{1.3}Al_{0.3}Ti_{1.7}(PO_4)_3$ as an electrolyte for solid lithium metal batteries, J. Energy Storage. 73 (2023) 108950, Doi: 10.1016/j.est.2023.108950.

[29] C. Miao, et al., LiF-doped $Li_{1.3}Al_{0.3}Ti_{1.7}(PO_4)_3$ superionic conductors with enhanced ionic conductivity for all-solid-state lithium-ion batteries, Ionics 28 (2022) 73–83, https://doi.org/10.1007/s11581-021-04324-2.

[30] X. Liang, et al., Plasma technology for advanced electrochemical energy storage, Chem Eur J 30 (2024) e202304168, https://doi.org/10.1002/chem.202304168.

[31] P. Liu, et al., Plasma coupled electrolyte additive strategy for construction of high-performance solid electrolyte interphase on Li metal anodes, Adv. Mater. 36 (2024) 2312812, https://doi.org/10.1002/adma.202312812.

[32] Z. Qiu, et al., Plasma enhanced lithium coupled with cobalt fibers arrays for advanced energy storage, Adv. Funct. Mater. 33 (2023) 2214987, https://doi.org/10.1002/adfm.202214987.

[33] Z. Gu, et al., Atomic-resolution electron microscopy unravelling the role of unusual asymmetric twin boundaries in the electron-beam-sensitive NASICON-type solid electrolyte, Nano Lett. 23 (2023) 11818–11826, https://doi.org/10.1021/acs.nanolett.3c03852.

[34] J. Shim, et al., Mixed electronic and ionic conductor-coated cathode material for high-voltage lithium ion battery, ACS Appl. Mater. Interfaces 8 (2016) 12205–12210, https://doi.org/10.1021/acsami.6b03113.

[35] S. Muto, et al., STEM-EELS spectrum imaging of an aerosol-deposited NASICON-type LATP solid electrolyte and LCO cathode interface, ACS Appl. Energ. Mater. 5 (2022) 98–107, https://doi.org/10.1021/acsaem.1c02512.

[36] Y. Yamamoto, Y. Iriyama, S. Muto, STEM-EELS analysis of the interface structures of composite ASS-LIB electrodes fabricated *via* aerosol deposition, J. Am. Ceram. Soc. 103 (2020) 1454–1462, https://doi.org/10.1111/jace.16813.

[37] A. Zollo, et al., Defect-mediated energy states in brookite nanorods: implications for photochemical applications under ultraviolet and visible light, J. Phys. Chem. C 128 (2024) 6971–6978, https://doi.org/10.1021/acs.jpcc.4c01066.

[38] Y. Wu, et al., Bifunctional TiO_{2x} nanofibers enhanced gel polymer electrolyte for high performance lithium metal batteries, J. Energy Chem. 89 (2024) 437–448, https://doi.org/10.1016/j.jechem.2023.09.049.

[39] O. Breuer, et al., Misuse of XPS in analyzing solid polymer electrolytes for lithium batteries, J. Electrochem. Soc. 171 (2024) 030510, https://doi.org/10.1149/1945-7111/ad2ef3.

[40] W. Slubowska, et al., B_2O_3-doped LATP glass-ceramics studied by X-ray diffractometry and MAS NMR spectroscopy methods, Nanomaterials 11 (2021) 19, https://doi.org/10.3390/nano11020390.

[41] C. Vinod Chandran, et al., Solid-state NMR investigations on the structure and dynamics of the ionic conductor $Li_{1+x}Al_xTi_{2}(PO_4)_3$ ($0.0 \leq x \leq 1.0$), J. Phys. Chem. C 120 (2016) 8436-8442, https://doi.org:10.1021/acs.jpcc.6b00318.

[42] E. Winter, et al., Nuclear magnetic resonance (NMR) studies of sintering effects on the lithium ion dynamics in $Li_{1.5}Al_{0.5}Ti_{1.5}(PO_4)_3$, Z, Phys. Chem. 236 (2022) 817–837, https://doi.org/10.1515/zpch-2021-3109.

[43] K. Kim, et al., Surface fluorination shielding of sulfide solid electrolytes for enhanced electrochemical stability in all-solid-state batteries, Adv. Mater. 37 (2025) 2416816, https://doi.org/10.1002/adma.202416816.

[44] D. Li, et al., A versatile InF_3 substituted argyrodite sulfide electrolyte toward ultrathin films for all-solid-state lithium batteries, Adv. Energy Mater. 14 (2024) 2402929, https://doi.org/10.1002/aenm.202402929.

[45] R. Wang, et al., Ion-conducting molecular-grafted sustainable cellulose quasi-solid composite electrolyte for high stability solid-state lithium-metal batteries, Adv. Funct. Mater. 34 (2024) 2402461, https://doi.org/10.1002/adfm.202402461.

[46] H. Xie, et al., Thermodynamic and kinetic behaviors of electrolytes mediated by intermolecular interactions enabling high-performance lithium-ion batteries, ACS Nano 18 (2024) 22503–22517, https://doi.org/10.1021/acsnano.4c07986.

[47] D. Lu, et al., Ligand-channel-enabled ultrafast Li-ion conduction, Nature 627 (2024) 101–107, https://doi.org/10.1038/s41586-024-07045-4.

[48] B. Xu, et al., Orderly arranged dipoles regulate anion-derived solid-electrolyte interphase for stable lithium metal chemistry, Adv. Mater. 36 (2024) 2311938, https://doi.org/10.1002/adma.202311938.

[49] Z. Wang, et al., 10 μm-thick high-strength solid polymer electrolytes with excellent interface compatibility for flexible all-solid-state lithium-metal batteries, Adv. Mater. 33 (2021) 2100353, https://doi.org/10.1002/adma.202100353.

[50] J. Chen, et al., Charging processes in lithium-oxygen batteries unraveled through the lens of the distribution of relaxation times, Chem 9 (2023) 2267–2281, https://doi.org/10.1016/j.chempr.2023.04.022.

[51] Y. Lu, et al., The timescale identification decoupling complicated kinetic processes in lithium batteries, Joule 6 (2022) 1172–1198, https://doi.org/10.1016/j.joule.2022.05.005.

[52] R. Chen, et al., Enhancing the thermal stability of NASICON solid electrolyte pellets against metallic lithium by defect modification, ACS Appl. Mater. Interfaces 13 (2021) 18743–18749, https://doi.org/10.1021/acsami.1c01246.

[53] M. Busche, et al., The formation of the solid/liquid electrolyte interphase (SLEI) on NASICON-type glass ceramics and LiPON, Adv. Mater. Interfaces 7 (2020) 2000380, https://doi.org/10.1002/admi.202000380.

[54] H. Tian, et al., Interfacial electronic properties dictate Li dendrite growth in solid electrolytes, Chem. Mat. 31 (2019) 7351–7359, https://doi.org/10.1021/acs.chemmater.9b01967.

[55] H. Zhang, D. Wang, C. Shen, In-situ EC-AFM and ex-situ XPS characterization to investigate the mechanism of SEI formation in highly concentrated aqueous

electrolyte for Li-ion batteries, Appl. Surf. Sci. 507 (2020) 145059, https://doi.org/10.1016/j.apsusc.2019.145059.
[56] Z. Yu, et al., Dendrites in solid-state batteries: ion transport behavior, advanced characterization, and interface regulation, Adv. Energy Mater. 11 (2021) 2003250, https://doi.org/10.1002/aenm.202003250.
[57] C. Liu, et al., Optimized layered ternary $LiNi_{0.5}Co_{0.2}Mn_{0.3}O_2$ cathode materials modified with ultrathin Li_3InCl_6 fast ion conductor layer for lithium-ion batteries, J. Power Sources. 566 (2023) 232961, Doi: 10.1016/j.jpowsour.2023.232961.
[58] Z. Chen, et al., $MnPO_4$-coated $Li(Ni_{0.4}Co_{0.2}Mn_{0.4})O_2$ for lithium(-ion) batteries with outstanding cycling stability and enhanced lithiation kinetics, Adv. Energy Mater. 8 (2018) 1801573, Doi: 10.1002/aenm.201801573.
[59] Z. Chen, et al., Manganese phosphate coated $Li[Ni_{0.6}Co_{0.2}Mn_{0.2}]O_2$ cathode material: Towards superior cycling stability at elevated temperature and high voltage, J. Power Sources 402 (2018) 263–271, https://doi.org/10.1016/j.jpowsour.2018.09.049.